Research Article Vol. 31, No. 19 / 11 Sep 2023 / Optics Express 31597
Optics EXPRESS

Simulated annealing algorithm with neural network for designing topological photonic crystals

YAODONG LIAO,[1,2] TIANEN YU,[1,2] YUEKE WANG,[1,2,3] BOXUAN DONG,[1,2] AND GUOFENG YANG[1,2,4]

[1] *Optical Information Science and Technology Department, Jiangnan University, Wuxi, Jiangsu 214122, China*
[2] *Optoelectronic Engineering and Technology Research Center, Jiangnan University, Wuxi, Jiangsu 214122, China*
[3] *ykwang@jiangnan.edu.cn*
[4] *gfyang@jiangnan.edu.cn*

Abstract: In this work, we utilize simulated annealing algorithm with neural network, to achieve rapid design of topological photonic crystals. We firstly train a high-accuracy neural network that predicts the band structure of hexagonal lattice photonic crystals. Subsequently, we embed the neural network into the simulated annealing algorithm, and choose the on-demand evaluation functions for optimizing topological band gaps. As examples, designing from the Dirac crystal of hexagonal lattice, two types of valley photonic crystals with the relative bandwidth of bandgap 26.8% and 47.6%, and one type of pseudospin photonic crystal with the relative bandwidth of bandgap 28.8% are obtained. In a further way, domain walls composed of valley photonic crystals (pseudospin photonic crystals) are also proposed, and full-wave simulations are conducted to verify the valley-locked (pseudospin-locked) edge states unidirectionally propagates under the excitation of circularly polarized source. Our proposed method demonstrates the efficiency and flexibility of neural network with simulated annealing algorithm in designing topological photonic crystals.

© 2023 Optica Publishing Group under the terms of the Optica Open Access Publishing Agreement

1. Introduction

Inspired by the quantum spin Hall effect (QSHE) and quantum valley Hall effect (QVHE) in graphene [1–5], researchers have demonstrated that topological photonic crystals (TPCs) originating from hexagonal lattice can simulate these quantum Hall effects without magnetic materials, advancing our knowledge of photonic topological insulators. Specifically, hexagonal lattice TPCs with C_6-symmetry exhibit QSHE [6–8], while those with reduced C_3-symmetry show QVHE [9,10]. The photonic systems with pseudospin or valley degree of freedom support pseudospin-locked or valley-locked chiral edge states at domain walls, which suppress backward scattering caused by disorder and abrupt bending. These topologically protected edge states have been verified experimentally [11–16] and applied to various devices, such as topologically protected photonic waveguides [14,17], terahertz communication [18–20], wave routing [21], beam splitter [22], topological laser [23–25] etc. However, the photonic devices based on topological edge states are often constrained by the range and width of the topological band gap. Therefore, optimizing the structure of photonic crystals to find the desired or wide topological band gap is a hot topic.

At present, some methods have been proposed to improve the design of TPCs, such as topological optimization [26–30], automatic differentiation and particle swarm algorithm [20,31,32]. These methods are used to obtain the optimal solution under constraints by essentially randomly updating parameters and iterating continuously, and require re-iteration for different optimization

#500720 https://doi.org/10.1364/OE.500720
Journal © 2023 Received 14 Jul 2023; revised 27 Aug 2023; accepted 27 Aug 2023; published 8 Sep 2023

Optics EXPRESS

objectives. However, the above mentioned methods are inefficient and usually fall into local optimal solutions when there are too many parameters. On the other hand, neural network as a data-driven method has shown superior performance in the design of optical artificial materials, such as predicting transmission of multilayer films and scattering spectra of nanoparticles [33–35], identifying and predicting resonant modes [36], designing TPCs [37–41], identifying topological invariants etc. [42,43]. This method trains a neural network to complete some specific tasks, and once the network is well trained, its response speed is several orders of magnitude higher than traditional methods [35]. This can not only accelerate the response speed of the above optimization process, but also help to rapidly explore topological band structures.

In this work, neural network combined with simulated annealing (SA) algorithm, is applied to the design of hexagonal lattice TPCs. A forward model (FM) based on the full connected neural network (NN) is firstly well trained, which can predict the photonic bands instantaneously. Subsequently, the on-demand evaluation functions are set, and the simulated annealing algorithm with forward model (SAFM) is used to find the optimized topological band gaps. Taking the Dirac crystal of hexagonal lattice as the beginning of the design, we demonstrate our design method with three typical cases, including two valley photonic crystals (VPC) and one pseudospin photonic crystals (PSPC), in which the relative bandwidth of bandgap can reach 26.8%, 47.6%, 28.8% respectively. The finite element method (FEM) results show that valley-locked (pseudospin -locked) edge states at domain walls of VPCs and DSPCs can be excited under chiral sources and propagate unidirectionally. Our findings pave a new way of designing topological photonic crystals efficiently and flexibly, by using a simulated annealing algorithm with neural network.

2. Design method, result, and discussion

2.1. Design space

It has been widely demonstrated that hexagonal photonic crystals can support QSHE and QVHE, which originate from the Dirac crystal [6–10]. Generally, the band structure can be modulated by designing the material distribution: 1) deforming the unit cell while preserving C_6-symmetry can open topological band gaps with QSHE; 2) further reducing the C_6-symmetry to C_3-symmetry can generate topological band gaps with QVHE. In this work, we use neural network (NN) to predict the bands structure of hexagonal photonic crystals, which are composed of six silicon cylinders (ε_{si} =13) arranged in air (ε_{air} = 1) as a unit cell, and one unit is as shown in the Fig. 1(a). We ensure that the hexagonal photonic crystals have C_3-symmetry, and those with C_6-symmetry can be regarded as a special case. Considering symmetry, we only need to focus our attention on the two silicon cylinders (C_1, C_2) in the rhombic region within the unit cell, and the rest of the unit cell can be obtained by rotating them. For constructing NN, the input space contains a total of six parameters as $\mathcal{D} = (x_1, y_1, r_1, x_2, y_2, r_2)$, where x_i, y_i, r_i are the x-axis coordinates, y-axis coordinates, and radii of the i_{th} (i = 1 and 2) silicon cylinder, respectively, which are normalized by the lattice constant a (= 240 nm). Here, we only consider TM modes for example, and calculate the first six bands along the high-symmetry boundaries of the first Brillouin zone (Γ-K-M-Γ) with finite element method(FEM). The number of wave vector along the high-symmetry boundaries is chosen as 30. Thus, the output space contains a total of 180 eigenfrequencies as $\mathcal{B} = (\omega_{1,1}, \ldots, \omega_{n,k}, \ldots, \omega_{6,30})$, and n(=1, 2, 3. . . 6) is the band index and k(=1, 2, 3. . . 30) is the wave vector index.

2.2. Neural networks for forward prediction

With proper network structure, hyperparameters and loss function, a neural network can be well trained based on a large enough training set, and a certain mapping relationship between the structure parameters of photonic crystal and the band structure can be constructed. Here, we train a forward model to fit the mapping function between the structural parameters $\mathcal{D}$ and the

Optics EXPRESS

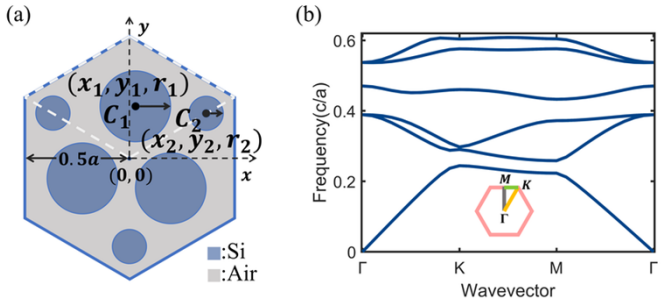

Fig. 1. Design space. (a) The unit cell constructed with Si (blue) and Air (grey) is controlled by $\mathcal{D} = (x_1, y_1, r_1, x_2, y_2, r_2)$. (b) Band structure including the first six bands, and the Brillouin zone is shown in the inset when $\mathcal{D} = (0.0278a, 0.2405a, 0.1658a, 0.3611a, 0.2084a, 0.0812a)$ for the schematic unit cell. 30 wave vectors are uniformly selected along the high-symmetry boundaries of the Brillouin zone.

band structure $\mathcal{B}$, noted as $\mathcal{F}$: $\mathcal{B}=\mathcal{F}(\mathcal{D})$. Therefore, the loss function is defined as:

$$MSELoss = \frac{1}{NK}\sum_{n,k}^{N,K}(\omega_{n,k,predicted} - \omega_{n,k,actual})^2 \tag{1}$$

where N and K are the number of photonic bands and wave vectors, respectively, which are 6 and 30 here. $\omega_{\mathrm{n,k,\ predicted}}$ and $\omega_{\mathrm{n,k,\ actual}}$ are the predicted and actual eigenfrequency. With adjusted hyperparameters, our well trained network is composed of 9 fully connected layers of 6-12-24-48-144-288-576-360-180, where the conventional activation function ReLU is applied after each layer, as shown in Fig. 2(a). The optimizer based on Adam algorithm modifies the weights of neurons more effectively during backpropagation, to improve the performance of network, which is used here with a learning rate of $3*10^{-4}$. In addition, a batch size of 32 is chosen, which achieves good performance.

We divide the data set (37000 sets) into training set and test set at a ratio of 5:1. The training set is used to train the network, and the test set is used to verify the network's generalizability and check whether overfitting occurred. The corresponding band structures are calculated by FEM based on COMSOL software. Forward model is trained for 500 epochs, and the curves of MSELoss are shown in Fig. 2(b). The lowest value of MSELoss for the training set and test set can reach about $4.1*10^{-6}$ and $4.8*10^{-6}$, respectively. The close performances between training set and test set indicate that the network not only accurately fits the mapping function $\mathcal{F}$, but also does not suffer from overfitting problem. We used a case outside the training set for comparing the predicted bands (PBs) and the actual bands (ABs), which are almost completely identical, as shown in Fig. 2(c). Thus, our forward model can output high-fidelity band structures. Meanwhile, the response time of well-trained forward model is less than 29μs per prediction, which is six orders of magnitude lower than those of FEM. Therefore, the high-fidelity and high-speed response ensures that it is feasible to utilize neural networks to achieve the prediction of the band structures of hexagonal photonic crystals, which provide a possible way to design the topological bandgaps with other optimization algorithms. More details can be found in Appendix A.

2.3. *Simulated annealing algorithm embedded with forward model*

Simulated annealing algorithm is an optimization method that relies on high-throughput search. This algorithm simulates the cooling process of metal to find the optimal solution, which involves three hyperparameters: initial temperature $\boldsymbol{T_{init}}$, stop temperature $\boldsymbol{T_{stop}}$, and annealing

Optics EXPRESS

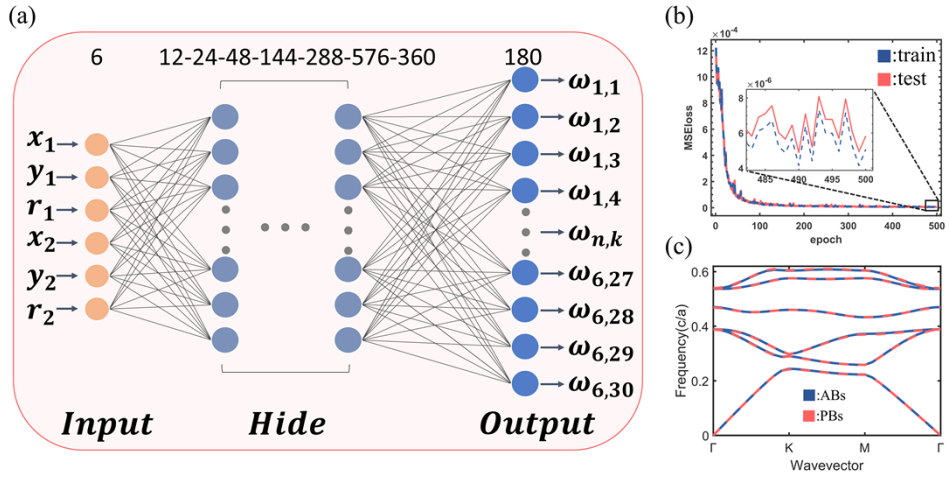

Fig. 2. Structure and result of the forward model. (a) The network structure consists of 9 fully connected layers, with node numbers of 6-12-24-48-144-288-576-360-180. ReLU activation function is applied after each layer and Adam optimizer is used with a learning rate of $3*10^{-4}$, and the training batch size is set as 32. (b) MSELoss of each epoch, blue dashed line and red line represent the MSEloss of the training set and test set, respectively. The inset shows the network performance of the last 20 epochs. (c) The predicted bands (red line) of the example structure shown in Fig. 1(a), which almost completely overlaps with the actual bands (blue line).

coefficient $\boldsymbol{\beta}$. In each round of optimization, the current temperature $\boldsymbol{T_{current}}$ is updated by $\boldsymbol{T_{current} = T_{current} \times \beta}$. Besides, this algorithm includes customizing the evaluation function $\boldsymbol{Eval}$, which is used to find the optimal solution to meet the optimization goal. In the design of hexagonal photonic crystals with topological band gaps, the calculations are usually based on FEM, whose response speed is slow when the search space is large. Here, we construct a simulated annealing algorithm with forward mode (SAFM) to accelerate the design, by taking the advantage of the fast response speed of forward model. In our design of photonic crystal band structures, the value of evaluation function is $\boldsymbol{Q}$ (= $\boldsymbol{Eval}(\mathcal{B})$),

The flow chart of SAFM is shown in Fig. 3. Firstly, the initial parameters $\mathcal{D}_{initial}$ (in the first loop, the current parameters $\mathcal{D}_{current}$ =$\mathcal{D}_{initial}$, and the current evaluation function $\boldsymbol{Q_{current} = Eval}(\mathcal{B}_{initial})$) of hexagonal photonic crystals are chosen and hyperparameters of SAFM are set. By neighborhood searching, a number of trial hexagonal photonic crystals with parameters $\mathcal{D}_{trial}$ are generated. Then the forward model is applied to predict the band structures $\mathcal{B}_{trial}$ of the trial hexagonal photonic crystals with the fast response speed. The evaluation function is employed, and $\boldsymbol{Q_{trial}}$(=$\boldsymbol{Eval}(\mathcal{B}_{trial})$) can be obtained for the trial solutions**.** To find the on-demand topological band gaps among the trial hexagonal photonic crystals, and the solution $\mathcal{D}_{new}$ with the highest $\boldsymbol{Q}_{\mathbf{new}}$ is chosen. Next, the SAFM updates the current structure parameters $\mathcal{D}_{current}$ according to the Metropolis criteria, which is based on a probability of $\boldsymbol{exp}\left(\frac{Q_{new}-Q_{current}}{T_{current}}\right)$, $\boldsymbol{T_{cuurent}}$ is the temperature of the current round. Finally, SAFM is stopped if the temperature $\boldsymbol{T_{current}}$ is lower than the stop temperature $\boldsymbol{T_{stop}}$**,** and the current solution $\mathcal{D}_{current}$ will be the output as the optimal solution $\mathcal{D}_{optimal}$; otherwise it loops from the neighborhood search. More details can be found in Appendix B.

Optics EXPRESS

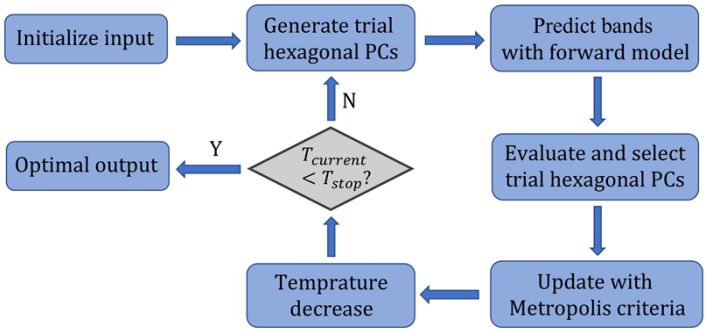

Fig. 3. The flow chart of simulated annealing algorithm with forward model.

2.4. *Starting point of designing TPC*

Keeping time-reversal symmetry, building topological band gaps can be achieved by breaking the space-reversal symmetry, which usually accompanies with band inversion. Therefore, the design of VPC and DSPC usually starts from the Dirac hexagonal photonic crystal, whose band structures have degenerate points at K, and four-fold degenerate points at Γ [6,10]. Here, the initial parameter $\mathcal{D}_{initial}$ is chosen as $\left(\frac{1}{6}a, \frac{\sqrt{3}}{6}a, \frac{3}{25}a, -\frac{1}{6}a, \frac{\sqrt{3}}{6}a, \frac{3}{25}a\right)$, as shown in Fig. 4(a), and the first six bands are plotted in Fig. 4(b). The degenerate points are 0.2923c/a and 0.5242c/a at K, and the four-fold degenerate point is 0.4393c/a at Γ. Implementing perturbations to the Dirac crystal can open different topological band gaps at K or Γ, and the optimal solution $\mathcal{D}_{optimal}$ can be easily obtained by SAFM.

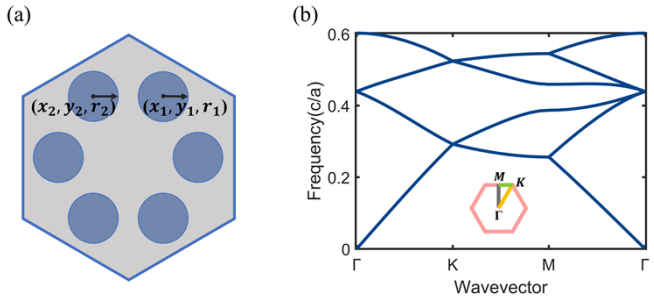

Fig. 4. Starting point of designing TPC. (a) The Dirac PC consists of six silicon cylinders (b), and the first six bands of (a).

2.5. *Design of TPCs with QVHE*

In this part, we start our design of TPCs with QVHE based on the previous studies [9,10]. The most-watched issue is constructing the topological edge states in TPCs, so we focus the design of VPCs with wide topological band gaps. As well known, the VPC of hexagonal photonic crystal can be achieved by breaking the degenerate Dirac point at K. Here, we use SAFM, chose the initial parameter $\mathcal{D}_{initial}$ as shown in part 2.4, and set the relative bandwidth of bandgap as evaluation function as below:

$$Q(n) = \frac{\Delta\omega_n}{\overline{\omega_n}} \tag{2}$$

Optics EXPRESS

Where $\Delta\omega_n$ refers to the width of the band gap between the n_{th} and $n+1_{th}$ band and $\overline{\omega_n}$ refers to the center frequency of the band gap.

Firstly, we break the degenerate Dirac point of Fig. 4(b) at 0.2923c/a, choose n as 2 in the Eq. (2), and aim to find the large topological band gap between the second and third band. By using SAFM (the details are shown in Appendix B), the relative bandwidth of bandgap reaches maximum after less than 30 rounds of search, as shown in Fig. 5(a). The unit cell structures with different parameters $\mathcal{D}$ in optimization process are also shown in the insets of Fig. 5(a). The optimal parameters of TPC are $\mathcal{D}_{optimal}$ =(0.0185a, 0.0913a, 0.0806a, -0.0135a, 0.4893a, 0.0768a), and the unit cell is shown in Fig. 5(b). Corresponding band structure is also draw in Fig. 5(b). The valley topological band gap ranges from 0.432 c/a to 0.566 c/a, is centered at 0.499 c/a and has the relative bandwidth of 26.8%. Phase profile of the eigen electrical field at the K point shows the clockwise (anticlockwise) rotation for the second (third) band, which verifies the valley topological properties of the band gap. Furthermore, we use the two VPCs with opposite valley Chern numbers of Fig. 5(b) to construct a zigzag interface, whose unit is shown in the right panel of Fig. 5(c). The left panel of Fig. 5(c) shows projected band structure, and the valley-locked edge states are drawn with blue lines, while the bulk states are gray. The eigen electrical field of the edge state at 0.512 c/a is depicted in Fig. 5(c), which is concentrated at the zigzag interface. We also build a domain wall structure composed of the two VPCs with opposite valley Chern numbers and $\mathcal{D}_{optimal}$. Full-wave simulation is conducted to observe valley-locked characteristic of topological edge states at 0.512 c/a, as shown in Fig. 5(d). Here, we set the excitation sources carrying positive (negative) orbital angular momentum at the center of the interface, and FEM simulations show that the valley-locked edge states unidirectionally propagate along the left (right) side, which demonstrates QVHE.

Also, we break another degenerate Dirac point of Fig. 4(b) at 0.5242c/a, choose n as 4 in the Eq. (2), and aim to find the valley topological band gap between the fourth and fifth band. By using SAFM, the relative bandwidth of bandgap reaches to 47.6% after less than 30 rounds of search, as shown in Fig. 6(a). The unit cell structures with different parameters $\mathcal{D}$ in cooling process are also shown in the insets of Fig. 6(a). The optimal parameters of VPC with largest bandgap are $\mathcal{D}_{optimal}$ = (-0.0079a, 0.2726a, 0.0736a, −0.4534a, 0.2734a, 0.0399a). The unit cell with $\mathcal{D}_{optimal}$ is shown in Fig. 6(b), and the corresponding band structure is also shown in Fig. 6(b). The valley topological band gap $\Delta\omega_4$ is centered at frequency 0.844 c/a and has the relative bandwidth of 47.6% (ranging from 0.643c/a to 1.045c/a). Phase profile of the eigen electric field at the K point shows the clockwise (anticlockwise) rotation for the fourth (fifth) band, which verifies the valley topological properties of the band gap. Furthermore, we use the two VPCs with opposite valley Chern numbers of Fig. 6(b) to construct a zigzag interface, whose unit is shown in the right panel of Fig. 6(c). The left panel of Fig. 6(c) shows projected band structure, the blue lines represent the valley-locked edge states, and gray region represent the bulk states. The eigen electric field of the edge state at 0.716 c/a is depicted in Fig. 6(c), which is concentrated at the zigzag interface. A domain wall structure, which is composed of the two VPCs with opposite valley Chern numbers and $\mathcal{D}_{optimal}$, is constructed. Electric field distribution shows that the valley-locked topological edge states at 0.716 c/a can be excited by sources carrying positive (negative) orbital angular momentum, and propagate unidirectionally along the left (right) side.

2.6. Design of TPCs with QSHE

Topological band gaps with QSHE can be achieved by breaking the four-fold degenerate point at Γ, and the pseudospin-locked edge states can be found at the interface between the topological nontrivial and trivial PCs. As discussed in study of Wu et al [6], the four-fold degenerate point of Fig. 4 can be opened by shrinking or expanding the six silicon cylinders, while keeping C_6-symmetry. Here, we choose n as 3 in Eq. (2), and aim to find the band gap between the

Optics EXPRESS

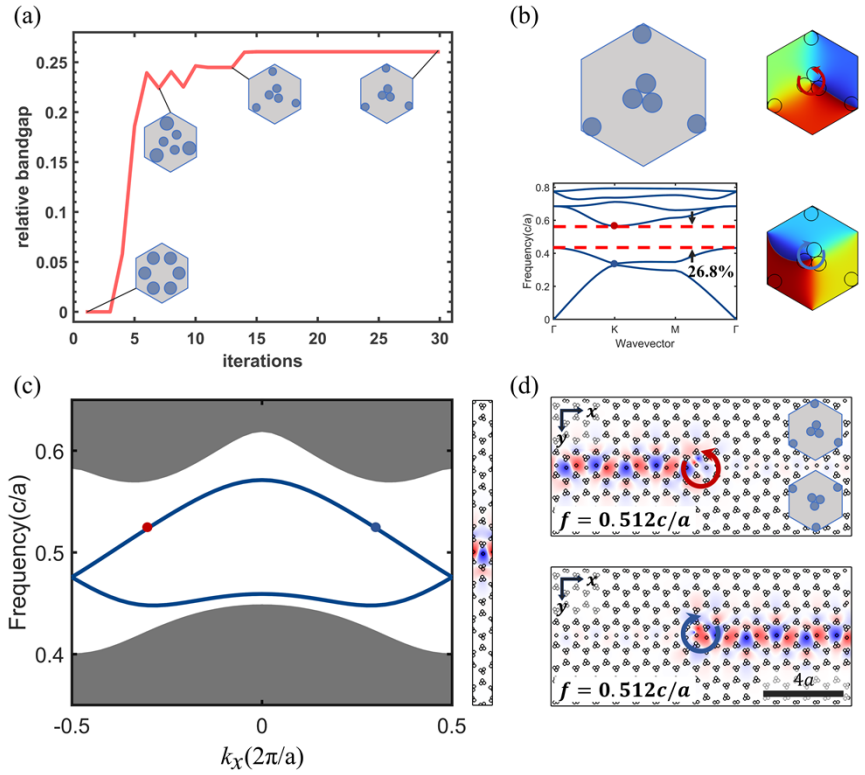

Fig. 5. Designed TPC with QVHE by SAFM. (a) The evaluation function in the iteration. The inset shows unit cell structures with different parameters $\mathcal{D}$. (b) Unit cell of VPC with $\mathcal{D}_{optimal}$ and the corresponding band structure. The phase profiles of second and third bands at K points, indicating the topological properties of the band gap. (c) The projected band structure (left panel) of the zigzag interface constructed by VPCs with opposite valley Chern numbers, and the eigen electrical field of the edge state at 0.512 *c/a* (right panel). (d) Electrical fields of valley-locked topological edge states excited by sources carrying positive (or negative) orbital angular momentum at 0.512 *c/a*.

third and fourth band. Firstly, we use SAFM to find the parameters $\mathcal{D}$ of TPC with expanded cylinders, for realizing the topological nontrivial band gap. In the optimization process, a number of solutions $\mathcal{D}_{trial}$ are randomly generated under the premise of maintaining C_6-symmetry. After less than 30 rounds of search, the relative bandwidth of bandgap reaches to 28.8% as shown in Fig. 7(d), and the unit cell structure is also shown in the insets of Fig. 7(a). The optimal parameters of topological nontrivial PC are $\mathcal{D}_{optimal}$ = (0.2057a, 0.3562a, 0.0873a, −0.2057a, 0.3562a, 0.0873a), and the unit cell structure is shown in Fig. 7(c). And the topological nontrivial band gap ranges from $f_{\mathbf{min}}$ (=0.457c/a) to $f_{\mathbf{max}}$ (=0.611c/a). Besides, the eigen electrical field of at Γ are shown as Fig. 7(e), which demonstrates that the second and third bands are quadrupole modes, and fourth and fifth bands are the dipole modes.

Then, we use SAFM to find the parameters $\mathcal{D}$ of hexagonal PC with shrunk cylinders, for realizing the topological trivial band gap. Maximizing the overlapped band gap between topological nontrivial and trivial PC, is to make sure constructing the pseudospin-locked edge states along the interface between them. For achieving this goal, we define Eq. (3) as the new

Optics EXPRESS

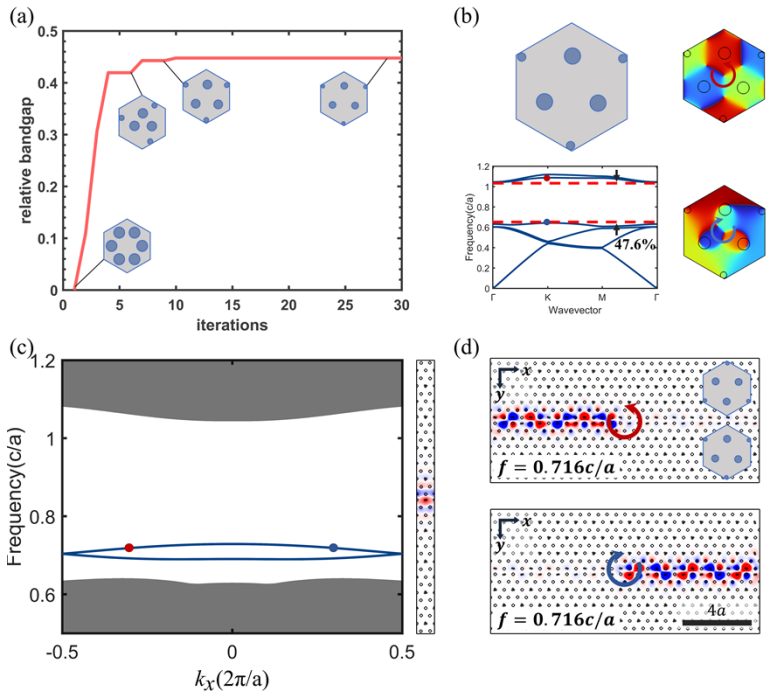

Fig. 6. Designed TPC with QVHE by SAFM. (a) The evaluation function varies in the iteration. The inset shows unit cell structures with different parameters $\mathcal{D}$. (b) Unit cell of VPC with $\mathcal{D}_{optimal}$ and the corresponding band structure. The phase profiles of fourth and fifth bands at K points. (c) The projected band structure (left panel) of the zigzag interface constructed by VPCs with opposite valley Chern numbers, and the eigen electric field of the edge state at 0.716 *c/a* (right panel). (d) Electrical fields of valley-locked topological edge states excited by chiral sources at 0.716 *c/a*.

evaluation function:

$$Q = \frac{f_{\max}' - f_{\min}' + f_{\max} - f_{\min} - |f_{\min}' - f_{\min}| - |f_{max}' - f_{max}|}{2(f_{min} + f_{\max})} \tag{3}$$

Here, $\boldsymbol{f_{\max}}$ and $\boldsymbol{f_{\min}}$ are the maximum and minimum frequencies of the topological nontrivial band gap respectively, which are shown in Fig. 7(d). $\boldsymbol{f_{\max}}$' and $\boldsymbol{f_{\min}}$' are the maximum and minimum frequencies of the topological trivial band gap.

In this optimization process of trivial PC, a number of solutions $\mathcal{D}_{trial}$ are also randomly generated under the premise of maintaining C_6-symmetry, and the evaluation function is based on Eq. (3). After less than 30 rounds of search, the relative bandwidth of bandgap reaches to 26.1% as shown in Fig. 7(g), and the unit cell structure in cooling process are also shown in the insets as shown in Fig. 7(b). The optimal parameters of trivial PC is $\mathcal{D}_{optimal}$ = (0.0962a, 0.1666a, 0.0962a, −0.0962a, 0.1666a, 0.0962a) for the topological trivial band gap, and the unit cell structure is shown in Fig. 7(f). And the topological trivial band gap ranges from $\boldsymbol{f_{\min}}$' (=0.467c/a) to $\boldsymbol{f_{\max}}$' (=0.607c/a). Besides, the eigen electric field of at Γ are shown as Fig. 7(h), which demonstrates that band inversion and topological transition happens, compared with the eigen electrical field in Fig. 7(e).

Optics EXPRESS

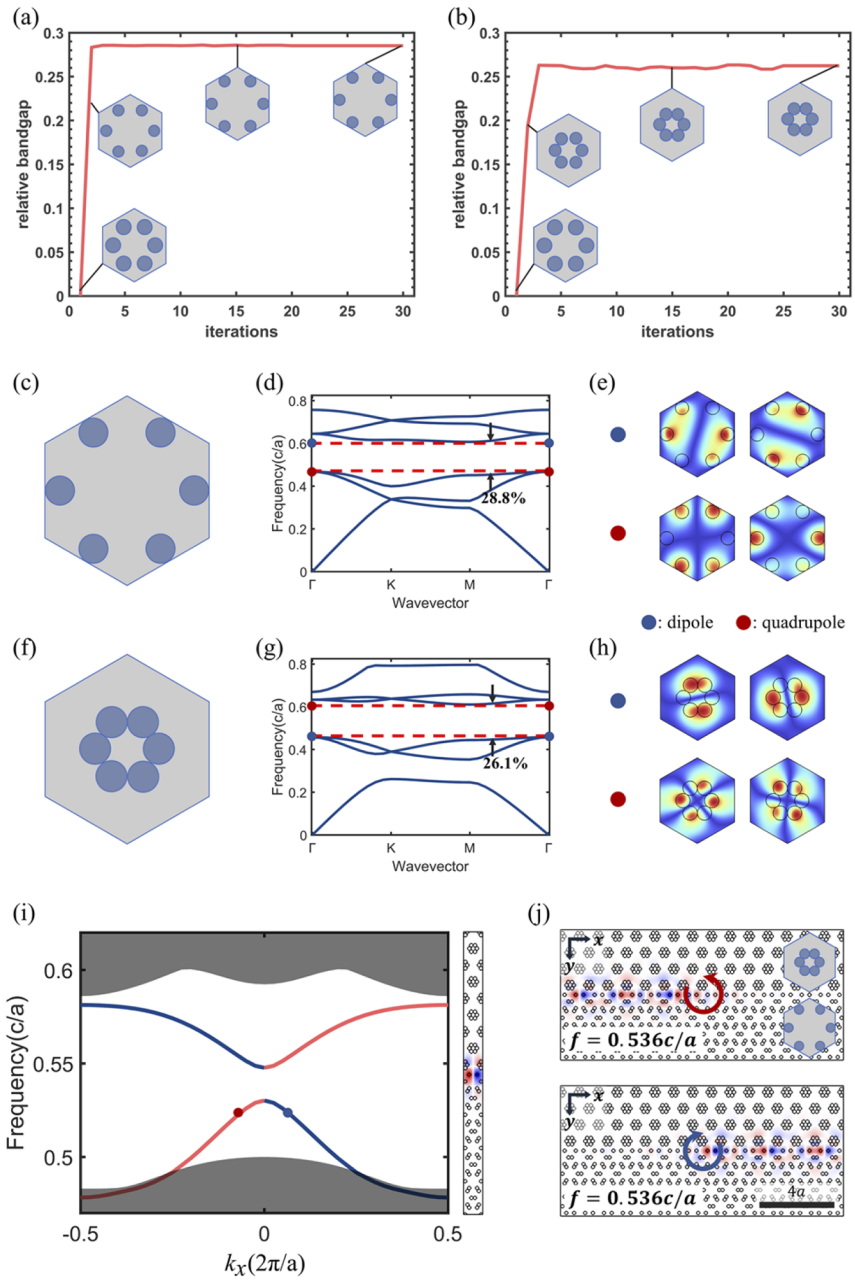

Fig. 7. Designed TPC with QSHE. The convergence process of the evaluation function for optimizing (a) topological nontrivial PC and (b) trivial PC. The inset shows unit cell structures during search process. (c) The unit cell and (d) band structure of topological nontrivial PC with $\mathcal{D}_{optimal}$. (e) The eigen electrical field of the second, third, fourth and fifth bands at Γ of topological nontrivial PC. (f) The unit cell and (g) band structure of topological trivial PC with $\mathcal{D}_{optimal}$. (h) The eigen electrical field of the second, third, fourth and fifth bands at Γ of topological trivial PC. (i) The projected band structure of the zigzag interface constructed by the topological nontrivial and trivial PC. The red and blue lines correspond to the pseudospin-up and pseudospin-down edge state modes, and band inversion of edge states happens at the $k_x = 0$. (j) Electric fields of the pseudospin-locked edge states under the chiral excitation source with frequency $f = 0.536c/a$.

Optics EXPRESS

We combine the topological nontrivial PC of Fig. 7(c) and trivial PC of Fig. 7(f) together to construct an interface structure, whose unit is shown in the right panel of Fig. 7(i). The left panel of Fig. 7(i) shows projected band structure, and the pseudospin-locked edge states are drawn with blue and red lines, while the bulk states are gray. The eigen electric field of the edge state at 0.536 *c/a* is depicted in the right panel of Fig. 7(i), which is concentrated at the interface. We also build a domain wall structure composed of the topological nontrivial and trivial PCs, which is shown in Fig. 7(j). Electric field distributions show that pseudospin-locked edge states unidirectionally propagate along the left (right) side under the excitation chiral sources carrying opposite orbital angular momentum, respectively. Except for the relative bandwidth of bandgap in our work, the evaluation function can be defined by different on-demand optimization goals, such as the central frequency of topological band gap, the range of topological band gap and so on. Besides, we have also conducted the optimization process by particle swarm algorithm with forward model (PSFM) for designing the above two types of valley photonic crystals and one type of pseudospin photonic crystal (shown in Supplement 1). For each case, the close topological bandgaps can be obtained by PSFM and SAFM, and the two methods achieve the optimal solutions after similar iterations. Therefore, it is believed that other optimization algorithms with forward model have also good performances in designing TPC.

3. Conclusion

Based on the Dirac hexagonal photonic crystal, we propose a simulated annealing algorithm with neural network for designing topological photonic crystals and edge states. The full connected neural network is firstly utilized to construct the forward model, which can which can predict the photonic bands quickly and accurately. Building the on-demand evaluation function for maximizing the relative bandwidth, SAFM can be achieved. Starting from Dirac hexagonal photonic crystal, the valley photonic band gaps with the relative bandwidth of 26.8% and 47.6%, and pseudo-spin photonic band gap with the relative bandwidth of 28.8% are obtained. FEM simulation results show that the valley-locked (pseudospin-locked) edge states can be excited under chiral sources and unidirectionally propagates along the domain wall. Our SAFM method paves a new way for designing topological photonic crystals with neural network, and can be easily extended to the other optimization problems of topological system.

Appendix A: data generating and computing resources

We use the random parameter generator to obtain the six parameters as $\mathcal{D} = (x_1, y_1, r_1, x_2, y_2, r_2)$, and filter the data making sure cylinders are within the rhombic region and not overlapping with each other. The band structures are calculated by FEM with COMSOL Multiphysics, the data of 37000 sets are performed on a cloud computer with AMD EPYC 7452 CPU 2.35 GHz, and it takes about 170 hours in total. Then, the band structure data are saved as a.csv file for subsequent neural network training. The neural network is implemented through the PyTorch library on Python and is also trained on the cloud computer, which takes about 43 minutes for the 9-layer network.

Appendix B: simulated annealing with forward model

Simulated Annealing is an optimization method used here to design topological photonic crystals with target topological band gaps, by maximizing the customized evaluation function. With solutions (i.e., structural parameters $\mathcal{D}$) representing hexagonal lattice topological photonic crystals, the SAFM is described as follows:

Optics EXPRESS

Initialization: Set initial temperature $T_{initial}$, stop temperature T_{stop}, annealing coefficient β

Define evaluation function $Eval$

Choose the initial solutions $\mathcal{D}_{initial}$

While $T_{current} < T_{stop}$:

Generate n trial solutions $\mathcal{D}_{trial}$ by randomly perturbing the current solutions $\mathcal{D}_{current}$ (in the first loop, $\mathcal{D}_{current}=\mathcal{D}_{initial}$ and $Q_{current}= Eval(\mathcal{B}_{initial})$)

Calculate the band structure $\mathcal{B}_{trial}$ of trial solutions $\mathcal{D}_{trial}$ with forward model $\mathcal{B}_{trial} = \mathcal{F}(\mathcal{D}_{trial})$

Evaluate the band structure of trial solutions, $Q_{trial} = Eval(\mathcal{B}_{trial})$

Select the local optimal solution $\mathcal{D}_{new}$ with the highest Q_{new} among the trial solutions

Update current solution according to Metropolis criteria:

if $Q_{new} > Q_{current}$:

Replace the current solution $\mathcal{D}_{current}$ with $\mathcal{D}_{new}$

else:

Select random number m from a uniform distribution of [0, 1]

if $exp(\frac{Q_{new} - Q_{current}}{T_{current}}) > m$:

Replace the current solution $\mathcal{D}_{current}$ with $\mathcal{D}_{new}$

else:

Remain the current solution $\mathcal{D}_{current}$

Temperature decrease, $T_{current} = \beta \times T_{current}$

Output the current solution $\mathcal{D}_{current}$ **as** the optional solution $\mathcal{D}_{optional}$

Where $T_{initial}$, T_{stop}, β are 1, $2*10^{-5}$, 0.7, respectively, and the number n of the trial solutions is 8000. The trial solutions $\mathcal{D}_{trial}$ is obtained from $\mathcal{D}_{current}$ by sampling with a uniform distribution ranging from [−0.5a, 0.5a]. We set critical values for the trial solutions $\mathcal{D}_{trial}$, ensuring cylinders are within the rhombic region and not overlapping with each other. In this work, each case converges to the optimal solution in less than 30 rounds of search, and each round of search takes less than one second.

Funding. Provincial College Students Innovation and Entrepreneurship Training Program of Jiangnan University (202210295184Y); National Natural Science Foundation of China (11404143).

Disclosures. The authors declare no conflicts of interest.

Data availability. Data underlying the results presented in this paper are not publicly available at this time but may be obtained from the authors upon reasonable request.

Supplemental document. See Supplement 1 for supporting content.

References

1. C. L. Kane and E. J. Mele, "Quantum spin Hall effect in graphene," Phys. Rev. Lett. **95**(22), 226801 (2005).
2. D. Xiao, W. Yao, and Q. Niu, "Valley-contrasting physics in graphene: Magnetic moment and topological transport," Phys. Rev. Lett. **99**(23), 236809 (2007).
3. A. F. Young, C. R. Dean, L. Wang, H. Ren, P. Cadden-Zimansky, K. Watanabe, T. Taniguchi, J. Hone, K. L. Shepard, and P. Kim, "Spin and valley quantum Hall ferromagnetism in graphene," Nat. Phys. **8**(7), 550–556 (2012).
4. A. F. Young, J. D. Sanchez-Yamagishi, B. Hunt, S. H. Choi, K. Watanabe, T. Taniguchi, R. C. Ashoori, and P. Jarillo-Herrero, "Tunable symmetry breaking and helical edge transport in a graphene quantum spin Hall state," Nature **505**(7484), 528–532 (2014).
5. L. Ju, Z. W. Shi, N. Nair, Y. C. Lv, C. H. Jin, J. Velasco, C. Ojeda-Aristizabal, H. A. Bechtel, M. C. Martin, A. Zettl, J. Analytis, and F. Wang, "Topological valley transport at bilayer graphene domain walls," Nature **520**(7549), 650–655 (2015).
6. L. H. Wu and X. Hu, "Scheme for Achieving a Topological Photonic Crystal by Using Dielectric Material," Phys. Rev. Lett. **114**(22), 223901 (2015).
7. S. Barik, H. Miyake, W. DeGottardi, E. Waks, and M. Hafezi, "Two-dimensionally confined topological edge states in photonic crystals," New J. Phys. **18**(11), 113013 (2016).
8. A. B. Khanikaev, S. H. Mousavi, W. K. Tse, M. Kargarian, A. H. MacDonald, and G. Shvets, "Photonic topological insulators," Nat. Mater. **12**(3), 233–239 (2013).

Optics EXPRESS

9. T. Ma and G. Shvets, "All-Si valley-Hall photonic topological insulator," New J. Phys. **18**(2), 025012 (2016).
10. X. D. Chen, F. L. Zhao, M. Chen, and J. W. Dong, "Valley-contrasting physics in all-dielectric photonic crystals: Orbital angular momentum and topological propagation," Phys. Rev. B **96**(2), 020202 (2017).
11. X. X. Wu, Y. Meng, J. X. Tian, Y. Z. Huang, H. Xiang, D. Z. Han, and W. J. Wen, "Direct observation of valley-polarized topological edge states in designer surface plasmon crystals," Nat. Commun. **8**(1), 1304 (2017).
12. J. Noh, S. Huang, K. P. Chen, and M. C. Rechtsman, "Observation of Photonic Topological Valley Hall Edge States," Phys. Rev. Lett. **120**(6), 063902 (2018).
13. Y. T. Yang, Y. F. Xu, T. Xu, H. X. Wang, J. H. Jiang, X. Hu, and Z. H. Hang, "Visualization of a Unidirectional Electromagnetic Waveguide Using Topological Photonic Crystals Made of Dielectric Materials," Phys. Rev. Lett. **120**(21), 217401 (2018).
14. X. T. He, E. T. Liang, J. J. Yuan, H. Y. Qiu, X. D. Chen, F. L. Zhao, and J. W. Dong, "A silicon-on-insulator slab for topological valley transport," Nat. Commun. **10**(1), 872 (2019).
15. N. Parappurath, F. Alpeggiani, L. Kuipers, and E. Verhagen, "Direct observation of topological edge states in silicon photonic crystals: Spin, dispersion, and chiral routing," Sci. Adv. **6**(10), eaaw4137 (2020).
16. B. Y. Xie, G. X. Su, H. F. Wang, F. Liu, L. M. Hu, S. Y. Yu, P. Zhan, M. H. Lu, Z. L. Wang, and Y. F. Chen, "Higher-order quantum spin Hall effect in a photonic crystal," Nat. Commun. **11**(1), 3768 (2020).
17. Y. T. Yang, H. Jiang, and Z. H. Hang, "Topological Valley Transport in Two-dimensional Honeycomb Photonic Crystals," Sci. Rep. **8**(1), 1588 (2018).
18. M. I. Shalaev, W. Walasik, A. Tsukernik, Y. Xu, and N. M. Litchinitser, "Robust topologically protected transport in photonic crystals at telecommunication wavelengths," Nat. Nanotechnol. **14**(1), 31–34 (2019).
19. Y. H. Yang, Y. Yamagami, X. B. Yu, P. Pitchappa, J. Webber, B. L. Zhang, M. Fujita, T. Nagatsuma, and R. Singh, "Terahertz topological photonics for on-chip communication," Nat. Photonics **14**(7), 446–451 (2020).
20. Y. J. Tan, W. H. Wang, A. Kumar, and R. Singh, "Interfacial topological photonics: broadband silicon waveguides for THz 6 G communication and beyond," Opt. Express **30**(18), 33035–33047 (2022).
21. G. C. Wei, Z. Z. Liu, D. S. Zhang, and J. J. Xiao, "Frequency dependent wave routing based on dual-band valley-Hall topological photonic crystal," New J. Phys. **23**(2), 023029 (2021).
22. L. He, H. Y. Ji, Y. J. Wang, and X. D. Zhang, "Topologically protected beam splitters and logic gates based on two-dimensional silicon photonic crystal slabs," Opt. Express **28**(23), 34015–34023 (2020).
23. Y. Q. Zeng, U. Chattopadhyay, B. F. Zhu, B. Qiang, J. H. Li, Y. H. Jin, L. H. Li, A. G. Davies, E. H. Linfield, B. L. Zhang, Y. D. Chong, and Q. J. Wang, "Electrically pumped topological laser with valley edge modes," Nature **578**(7794), 246–250 (2020).
24. Z. K. Shao, H. Z. Chen, S. Wang, X. R. Mao, Z. Q. Yang, S. L. Wang, X. X. Wang, X. Hu, and R. M. Ma, "A high-performance topological bulk laser based on band-inversion-induced reflection," Nat. Nanotechnol. **15**(1), 67–72 (2020).
25. Y. K. Gong, S. Wong, A. J. Bennett, D. L. Huffaker, and S. S. Oh, "Topological Insulator Laser Using Valley-Hall Photonic Crystals," ACS Photonics **7**(8), 2089–2097 (2020).
26. R. E. Christiansen, F. W. Wang, O. Sigmund, and S. Stobbe, "Designing photonic topological insulators with quantum-spin-Hall edge states using topology optimization," Nanophotonics **8**(8), 1363–1369 (2019).
27. Y. F. Chen, F. Meng, Y. Kivshar, B. H. Jia, and X. D. Huang, "Inverse design of higher-order photonic topological insulators," Phys. Rev. Res. **2**(2), 023115 (2020).
28. Y. F. Chen, F. Meng, B. H. Jia, G. Y. Li, and X. D. Huang, "Inverse Design of Photonic Topological Insulators with Extra-Wide Bandgaps," Phys. Status Solidi RRL **13**(9), 1900175 (2019).
29. R. E. Christiansen, F. W. Wang, and O. Sigmund, "Topological Insulators by Topology Optimization," Phys. Rev. Lett. **122**(23), 234502 (2019).
30. Y. F. Chen, F. Meng, J. Zhu, and X. D. Huang, "Inverse design of second-order photonic topological insulators in C-3-symmetric lattices," Appl. Math. Model. **102**, 194–206 (2022).
31. E. Nussbaum, E. Sauer, and S. Hughes, "Inverse design of broadband and lossless topological photonic crystal waveguide modes," Opt. Lett. **46**(7), 1732–1735 (2021).
32. M. Minkov, I. A. D. Williamson, L. C. Andreani, D. Gerace, B. C. Lou, A. Y. Song, T. W. Hughes, and S. H. Fan, "Inverse Design of Photonic Crystals through Automatic Differentiation," ACS Photonics **7**(7), 1729–1741 (2020).
33. Y. R. Qu, L. Jing, Y. C. Shen, M. Qiu, and M. Soljacic, "Migrating Knowledge between Physical Scenarios Based on Artificial Neural Networks," ACS Photonics **6**(5), 1168–1174 (2019).
34. C. K. Qiu, X. Wu, Z. Luo, H. D. Yang, G. N. He, and B. Huang, "Nanophotonic inverse design with deep neural networks based on knowledge transfer using imbalanced datasets," Opt. Express **29**(18), 28406–28415 (2021).
35. J. Peurifoy, Y. C. Shen, L. Jing, Y. Yang, F. Cano-Renteria, B. G. DeLacy, J. D. Joannopoulos, M. Tegmark, and M. Soljacic, "Nanophotonic particle simulation and inverse design using artificial neural networks," Sci. Adv. **4**(6), eaar4206 (2018).
36. X. Z. Ma, Y. Ma, P. Cunha, Q. S. Liu, K. Kudtarkar, D. Xu, J. F. Wang, Y. X. Chen, Z. J. Wong, M. Liu, M. C. Hipwell, and S. F. Lan, "Strategical Deep Learning for Photonic Bound States in the Continuum," Laser Photonics Rev. **16**(10), 2100658 (2022).
37. Y. Long, J. Ren, Y. H. Li, and H. Chen, "Inverse design of photonic topological state via machine learning," Appl. Phys. Lett. **114**(18), 181105 (2019).

Optics EXPRESS

38. L. Pilozzi, F. A. Farrelly, G. Marcucci, and C. Conti, "Machine learning inverse problem for topological photonics," Commun. Phys. **1**(1), 57 (2018).
39. R. Singh, A. Agarwal, and B. W. Anthony, "Mapping the design space of photonic topological states via deep learning," Opt. Express **28**(19), 27893–27902 (2020).
40. Z. L. Du, X. G. Ding, H. Chen, C. Liu, W. S. Zhang, J. C. Luo, and X. Guo, "Optimal design of topological waveguides by machine learning," Front. Mater. **9**, 1075073 (2022).
41. T. Christensen, C. Loh, S. Picek, L. Jing, S. Fisher, V. Ceperic, J. D. Joannopoulos, M. Soljacic, and D. Jakobovic, "Predictive and generative machine learning models for photonic crystals," Nanophotonics **9**(13), 4183–4192 (2020).
42. N. Sun, J. M. Yi, P. F. Zhang, H. T. Shen, and H. Zhai, "Deep learning topological invariants of band insulators," Phys. Rev. B **98**(8), 085402 (2018).
43. P. F. Zhang, H. T. Shen, and H. Zhai, "Machine Learning Topological Invariants with Neural Networks," Phys. Rev. Lett. **120**(6), 066401 (2018).